

Descriptor-Based Classification of Interfacial Electronic Coupling in Janus XP_3 -Based 2D Heterostructures

Erika N. Lima^{a,b}, Teldo A. S. Pereira^{a,b}, Elisangela S. Barboza^a, Dominike Pacine^c, Igor S. S. de Oliveira^d

^a*Instituto de Física, Universidade Federal de Mato Grosso, Cuiabá, 78060-900, MT, Brazil*

^b*National Institute of Science and Technology on Materials Informatics, Campinas, SP, Brazil*

^c*Instituto Federal de Educação, Ciência e Tecnologia do Triângulo Mineiro, Uberlândia, 38064-190, MG, Brazil*

^d*Departamento de Física, Universidade Federal de Lavras, Lavras, 37203-202, MG, Brazil*

Abstract

Understanding and controlling interfacial electronic coupling in two-dimensional (2D) heterostructures is essential for designing functional materials for electronic, optoelectronic, and catalytic applications. Here, we investigate vertical heterobilayers constructed from two distinct XP_3 monolayers ($X = \text{As}, \text{Ge}, \text{Sb}, \text{Bi}, \text{Sn}, \text{Al}, \text{Ga}, \text{and Pb}$) using first-principles density functional theory. The resulting Janus heterobilayers are energetically favorable and elastically stable, with electronic band gaps ranging from metallic and near-metallic to semiconducting regimes. Interlayer interactions induce significant band renormalization, including transitions between type-I and type-II alignment upon structural relaxation. To rationalize these effects, we establish a descriptor-based framework based on the metal-metal interlayer distance, interfacial electron localization, and Bader charge redistribution. This combined analysis discriminates vdW-like, polar-covalent, and ionic interaction regimes, with systematic trends governed by the average atomic number of the constituent elements. Optical absorption calculations indicate visible-to-near-infrared activity in selected systems, and band-edge alignment identifies promising candidates for selective redox processes. Overall, the proposed descriptor-based strategy provides a physically grounded route for

*Corresponding author

Email address: erika.lima@fisica.ufmt.br (Erika N. Lima)

identifying and engineering interfacial coupling in XP_3 heterostructures and can be extended to other classes of 2D material interfaces.

Keywords:

2D materials, XP_3 heterostructures, Janus materials, van der Waals heterostructures, interfacial electronic coupling, density functional theory

1. Introduction

Two-dimensional (2D) materials provide a versatile platform for engineering interfacial electronic properties through vertical stacking. In such heterostructures, the electronic response is governed by the nature of the interlayer interaction, which controls charge redistribution, band alignment, and carrier separation. Although many 2D systems are described as weakly coupled by van der Waals (vdW) forces, this approximation is not universally valid, as the interaction regime depends on chemical composition and interlayer geometry. [1]

Among emerging 2D materials, triphosphides with general formula XP_3 , where X belongs to groups 13–16 and P denotes phosphorus, form a structurally robust and chemically versatile family. Their puckered lattice geometry ensures structural stability, while their electronic properties vary significantly with the identity of X, enabling tunable band gaps, carrier mobility, and optical response. [2, 3, 4] Representative members such as GeP_3 , SnP_3 , and SbP_3 exhibit narrow band gaps, strong optical absorption, and high carrier mobility. Experimental realization of bulk layered GeP_3 and SnP_3 , as well as few-layer nanosheets, further supports the viability of this materials family.[5, 6, 7, 8]

Recent studies have extended XP_3 materials to heterostructure architectures. Oliveira et al. demonstrated that few-layer BiP_3 enables Schottky barrier modulation in graphene-based vdW heterostructures.[9] Lu et al. investigated vertical and lateral XP_3 heterostructures, identifying AlP_3/GaP_3 as a promising photocatalytic system. [10] However, a systematic and physically grounded framework capable of classifying interfacial electronic coupling in heterobilayers composed exclusively of XP_3 monolayers is still lacking, as interlayer separation alone is insufficient to classify the interaction regime.

To address this gap, we employ first-principles calculations based on the Density Functional Theory (DFT) to investigate vertical heterobilayers formed by stacking two distinct XP_3 monolayers ($X_A P_3/X_B P_3$). These heterobilayers exhibit a Janus character as a result of compositional asymmetry between the

layers, generating non-equivalent interfacial environments. To ensure realistic and experimentally viable systems, our analysis is restricted to thermally and dynamically stable monolayers, namely AsP₃, GeP₃, SbP₃, BiP₃, SnP₃, AlP₃, GaP₃, and PbP₃.

Here, we establish a descriptor-based framework that quantitatively links geometric and electronic descriptors to the strength and character of interfacial electronic coupling in XP₃ heterobilayers. The metal–metal interlayer distance serves as the primary geometric descriptor, while interfacial electron localization and Bader charge redistribution capture electronic sharing and charge transfer across the interface. Their combined analysis enables discrimination among vdW-like, polar–covalent, and ionic interaction regimes, with deviations from simple distance-based trends rationalized by the average atomic number of the constituent elements. In addition, the physically interpretable descriptors introduced here may provide suitable input features for future data-driven or machine-learning approaches aimed at the rapid screening of heterobilayers.

In addition to classifying interfacial coupling, we analyze mechanical properties, optical absorption spectra, and band-edge alignment relevant to redox processes. Together, these findings provide a rational design roadmap for constructing XP₃ heterobilayers with controlled interfacial interaction regimes and tailored functional properties. The descriptor-based strategy proposed here may be extended to other 2D heterostructures in which interlayer electronic coupling plays a central role, provided that the specific chemical and structural characteristics of each system are properly considered.

2. Computational Method

All structural and electronic properties in the present work were calculated using first-principles methods based on Density Functional Theory (DFT),^[11, 12] as implemented in the Vienna *ab initio* Simulation Package (VASP).^[13] The exchange–correlation potential was described within the generalized gradient approximation (GGA) using the Perdew–Burke–Ernzerhof (PBE) functional. The interactions between valence electrons and ionic cores were treated using the projector augmented wave (PAW) method.^[14, 15] Long-range dispersive interactions were included through the semiempirical DFT-D3 correction scheme proposed by Grimme.^[16] This approach provides an accurate description of dispersive forces governing the interlayer binding in layered heterostructures.

The electronic wave functions were expanded in a plane-wave basis set with an energy cutoff of 500 eV. Brillouin zone integrations were performed using a $10 \times 10 \times 1$ Γ -centered Monkhorst–Pack k -point mesh.[17] Structural models were constructed using periodic supercells in the xy -plane, with a vacuum region of approximately 15 Å introduced along the z -direction to avoid spurious interactions between periodic images. A dipole correction along the out-of-plane direction was applied to eliminate artificial electrostatic interactions arising from the asymmetric slab geometry. Structural relaxations were performed using a conjugate-gradient algorithm until the total energy converged to within 10^{-6} eV and the residual forces on each atom were below 0.01 eV/Å. To minimize strain effects and ensure structural compatibility, the lattice mismatch between the stacked monolayers was constrained to a maximum of 2%, symmetrically distributed between the two constituent layers during structural optimization.

To obtain more accurate electronic band gaps, the electronic band structures were subsequently recalculated using the screened Heyd–Scuseria–Ernzerhof (HSE06) hybrid functional, [18, 19] including spin–orbit coupling (SOC) effects. In these calculations, 25% of the short-range Hartree–Fock exact exchange was incorporated into the PBE exchange, employing the standard screening parameter of 0.2 \AA^{-1} .

The optical properties of the XP_3 heterobilayers were investigated using the WanTiBEXOS code. [20] The Tight-Binding (TB) Hamiltonian was constructed based on the first-principles electronic structure, obtained via the HSE06 hybrid functional using the interface between the VASP and Wannier90 packages. [21] Maximally Localized Wannier Functions (MLWFs) were generated by considering the projections of the s , p , and d orbitals of the XP_3 heterobilayers. Regarding the interaction model, a truncated Coulomb potential for 2D systems (V2DT) [22] was adopted, with a k -point mesh density of 120 \AA^{-1} . For the real and imaginary parts of the dielectric function, a broadening parameter of 0.01 eV was used. The optical spectra were computed in the energy range from 0 to 4 eV, including the eight highest valence bands (n_v) and the eight lowest conduction bands (n_c). Finally, the optical properties were analyzed at both the Independent Particle Approximation (IPA) level and within the Bethe–Salpeter Equation (BSE) formalism, [23] which explicitly accounts for excitonic effects.

Monolayer	a (Å)	h (Å)	E_g (eV)
AlP ₃	7.21	1.39	1.50
GaP ₃	7.21	1.22	1.51
GeP ₃	6.96	2.40	0.59
SnP ₃	7.15	2.85	0.74
PbP ₃	7.28	2.96	0.86
AsP ₃	6.73	1.49	2.61
SbP ₃	7.00	1.79	2.34
BiP ₃	7.13	1.94	2.05

Table 1: In-plane lattice constant a , monolayer thickness h , and electronic band gap E_g calculated for dynamically and thermally stable XP₃ isolated monolayers.

3. Results and Discussion

3.1. Structural and Energetic Properties

We begin our investigation by constructing the individual XP₃ monolayers, where X = As, Ge, Sb, Bi, Sn, Al, Ga, and Pb. All systems adopt a puckered hexagonal honeycomb lattice, consistent with prior theoretical predictions for this class of materials. [24] After relaxation, we extracted the equilibrium in-plane lattice constant (a) and the monolayer thickness (h), defined as the vertical distance between the outermost atoms. Additionally, we calculated the electronic band gap (E_g) of each system. The calculated structural parameters and electronic band gaps are summarized in Table 1. The lattice parameter and monolayer thickness increase with the atomic radius of X, with a ranging from 6.73 Å (AsP₃) to 7.28 Å (PbP₃), and h from 1.49 to 2.96 Å for the same compounds. The band gaps span a wide range, from 0.59 eV in GeP₃ to 2.61 eV in AsP₃, highlighting the tunability of the electronic properties across the XP₃ series. These results are consistent with previous work. [25]

To construct structurally and energetically viable X_AP₃/X_BP₃ heterobilayers, we systematically evaluated the lattice mismatch between all possible pairs of monolayers considered in this study. Only combinations exhibiting a lattice mismatch below approximately 2.0% were selected, ensuring mechanical compatibility and minimizing interfacial strain in the resulting heterostructures. To further preserve structural symmetry and avoid the concentration of strain in a single layer, the total lattice mismatch was symmetrically distributed between the two monolayers during structural optimization. Based on these

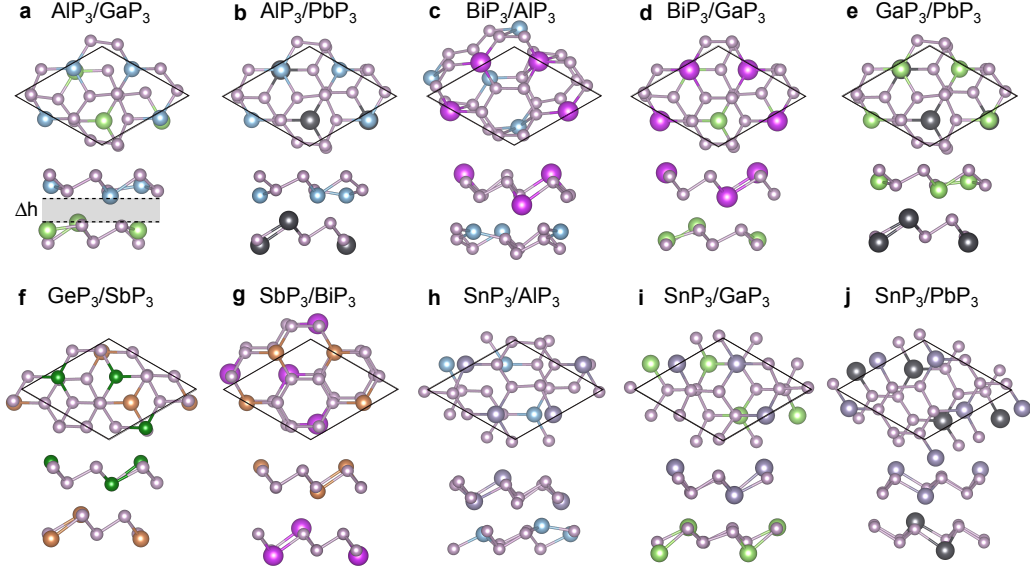


Figure 1: Top and side views of the optimized atomic structures of the investigated Janus XP_3 heterobilayers: (a) AlP_3/GaP_3 , (b) AlP_3/PbP_3 , (c) BiP_3/AlP_3 , (d) BiP_3/GaP_3 , (e) GaP_3/PbP_3 , (f) GeP_3/SbP_3 , (g) SbP_3/BiP_3 , (h) SnP_3/AlP_3 , (i) SnP_3/GaP_3 , and (j) SnP_3/PbP_3 . The dashed line represents the interlayer distance Δh , defined as the vertical separation between the metal atoms located at the centers of the two opposite layers forming the heterobilayer. The atomic species are identified by the following color code: light blue for Al, light green for Ga, dark gray for Pb, magenta for Bi, dark green for Ge, orange for Sb, purple for Sn, and light pink for P.

criteria, we selected ten representative $X_A P_3/X_B P_3$ heterostructures for detailed investigation. These systems span a broad range of lattice mismatch values, from virtually strain-free configurations such as AlP_3/GaP_3 (0.00%) to moderate mismatch systems like SnP_3/PbP_3 (1.79%) and SbP_3/BiP_3 (1.82%). The smallest mismatches are found in heterostructures such as GeP_3/SbP_3 (0.57%) and SnP_3/GaP_3 (0.83%), which are expected to exhibit minimal strain-induced distortions and high interfacial quality. On the other hand, even heterostructures with larger mismatch values remain within acceptable limits for theoretical modeling. The complete list of lattice mismatch values for all investigated XP_3 heterostructures is presented in Table 2.

The binding energies of the heterobilayers are computed according to

$$E_b = (E_{\text{het}} - E_{X_A P_3} - E_{X_B P_3})/S, \quad (1)$$

where E_{het} and $E_{X_A/B P_3}$ denote the total energies of the heterostructure and

Heterobilayers	strain (%)	Δh (Å)	E_b (meV/Å ²)	E_g (eV)	$\Delta\rho$ (10 ¹³ e/cm ²)	$d_{X_A X_B}$ (Å)	ELF _{mid} (-)	\bar{Z} (-)
AlP ₃ /GaP ₃	0.00	1.85	-143.5	0.35	9.61	2.94	0.30	18.0
AlP ₃ /PbP ₃	0.96	1.83	-141.5	0.67	14.40	3.55	0.03	47.5
BiP ₃ /AlP ₃	1.11	1.77	-121.3	0.61	5.92	3.42	0.31	48.0
BiP ₃ /GaP ₃	1.11	2.01	-125.3	-	1.53	4.59	0.02	57.0
GaP ₃ /PbP ₃	0.96	2.00	-131.6	0.09	3.09	4.64	0.02	56.5
GeP ₃ /SbP ₃	0.57	2.04	-140.1	0.11	3.57	2.92	0.60	41.5
SbP ₃ /BiP ₃	1.82	2.66	-109.7	1.11	0.46	5.82	0.23	67.0
SnP ₃ /AlP ₃	0.83	1.74	-141.3	0.89	16.60	2.69	0.22	32.5
SnP ₃ /GaP ₃	0.83	2.26	-136.2	-	1.46	4.24	0.02	41.5
SnP ₃ /PbP ₃	1.79	1.89	-129.6	-	0.90	3.28	0.23	66.0

Table 2: Properties of representative XP₃ heterostructures: lattice mismatch (strain), interlayer spacing (Δh), interlayer binding energy (E_b), electronic band gap (E_g), equilibrium interlayer distance between the metals X_A and X_B ($d_{X_A X_B}$), electron localization function evaluated at the metal-metal midpoint (ELF_{mid}), and the average atomic number \bar{Z} , which is defined as $\bar{Z} = (Z_{X_A} + Z_{X_B})/2$.

the isolated XP₃ monolayers, respectively, and S is the supercell area. Several initial stacking configurations between the two monolayers were considered. The results corresponding to the most stable E_b values are presented in Table 2, and the optimized structures are depicted in Fig. 1. Table 2 shows that XP₃ heterobilayers exhibit strong interlayer binding energies, with adsorption energies ranging from -129.6 meV/Å² (SbP₃/BiP₃) to -143.5 meV/Å² (AlP₃/GaP₃), a variation of $\sim 10\%$. The corresponding interlayer spacings vary between 1.74 and 2.66 Å, reflecting subtle differences in atomic size and orbital overlap across the different structures. Heterostructures involving lighter elements (e.g., Al, Ga) tend to exhibit shorter separations, consistent with stronger binding, while those containing heavier elements (e.g., Sb, Bi) show larger spacings and weaker interactions.

3.2. Electronic Properties

Next, we investigate the charge transfer (CT) between the monolayers in the XP₃ heterostructures. We use the Bader charge analysis [26, 27] to compute the net charge gain or loss of each XP₃ layer, which was obtained by summing the Bader charges of all atoms belonging to a given layer in the heterostructure and subtracting the corresponding charge of the isolated free-standing XP₃ monolayer. The differential charge density $\Delta\rho$ was then

calculated by normalizing the resulting difference by the in-plane supercell area S .

The results for $\Delta\rho$ presented in Table 2 reveal systematic trends that complement understanding of the variations in interlayer binding energies and interlayer spacings across the $X_A P_3/X_B P_3$ heterostructures. The interfaces involving AlP_3 show the largest charge redistribution, with densities reaching $9.6 \times 10^{13} - 1.7 \times 10^{14} e/cm^2$ when paired with GaP_3 , PbP_3 , and SnP_3 . These values correlate directly with the strongest interlayer binding observed in the series, between -143.5 to -141.3 meV/Å², which also display shorter interlayer distances ($\sim 1.7 - 1.9$ Å). This indicates that stronger orbital coupling at small separations is supported by modest but significant electron redistribution at the interface.

By contrast, heterostructures composed of combinations of monolayers with heavier elements, such as BiP_3 , SbP_3 , SnP_3 , and PbP_3 exhibit much smaller CT densities, such as the BiP_3/SbP_3 interface ($4.6 \times 10^{12} e/cm^2$) and the SnP_3/PbP_3 interface ($9.0 \times 10^{12} e/cm^2$), both of which correspond to larger interlayer spacings and weaker interlayer binding energies. These reduced values reflect the more ideal vdW character of the interaction, where limited orbital overlap leads to minimal charge redistribution.

In Fig. 2, we present the band-edge positions of the XP_3 monolayers together with those of the investigated $X_A P_3/X_B P_3$ heterostructures. In several cases, the direction of charge transfer follows the trend expected from the ionization energy (IE) differences, with electrons consistently flowing from layers with lower IE (donors) to those with higher IE (acceptors). This behavior is observed, for example, in heterostructures where GaP_3 receives electrons from AlP_3 , BiP_3 , or SnP_3 . However, in other systems, charge transfer (CT) does not follow the trend predicted by the IE differences, such as in the heterostructures formed by AlP_3 with PbP_3 , BiP_3 , or SnP_3 , as well as PbP_3 combined with GaP_3 or SnP_3 . These deviations indicate that the direction and magnitude of charge transfer are primarily governed by interfacial phenomena, particularly orbital hybridization, chemical bonding strength, and the formation of interface dipoles. In general, the observed CT behavior reveals that interfaces exhibiting larger electron redistribution tend to show stronger interlayer binding and shorter equilibrium separations, while systems with minimal charge transfer correspond to weak, predominantly vdW-coupled heterostructures.

The XP_3 heterobilayers exhibit a wide range of band gaps, as presented in Table 2, spanning from metallic (BiP_3/GaP_3 , SnP_3/GaP_3 , SnP_3/PbP_3)

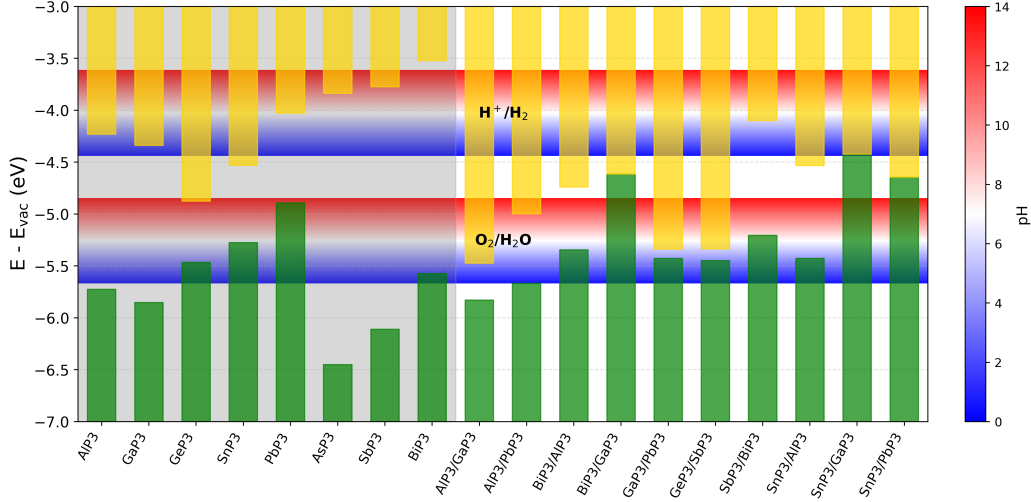


Figure 2: Band edge alignment of the monolayers and heterostructures relative to the vacuum level ($E - E_{\text{vac}}$). The yellow bars represent the conduction band minimum (E_{CBM}), and the green bars correspond to the valence band maximum (E_{VBM}). The horizontal colored regions indicate the redox potentials of water, with the upper band corresponding to the H^+/H_2 level and the lower band to the $\text{O}_2/\text{H}_2\text{O}$ level. The color map represents the pH dependence of the redox potentials, varying continuously from pH 0 (blue) to pH 14 (red), as described by the Nernst equations 2 and 3.

and nearly-metallic values of 0.09–0.11 eV in $\text{GaP}_3/\text{PbP}_3$ and $\text{GeP}_3/\text{SbP}_3$ to semiconducting gaps close to 1.1 eV in $\text{SbP}_3/\text{BiP}_3$. In general, stacking reduces the band gap relative to the isolated monolayers (0.59–2.61 eV), reflecting enhanced interlayer hybridization. The most pronounced narrowing occurs in heterostructures containing heavier elements such as Sn, Pb, and Bi, where strong orbital overlap and SOC favor charge delocalization. Conversely, combinations that pair lighter (Al, Ga, As) with heavier elements retain intermediate gaps of 0.6–0.9 eV, balancing carrier transport with infrared optical activity. Altogether, the results demonstrate that XP_3 heterostructures provide a versatile platform where the electronic band gap can be tuned from a near-metallic regime to the visible–IR range, enabling potential applications in low-power electronics, and optoelectronics.

3.3. Interlayer Interaction Regimes

While the previous sections established systematic trends in binding energy and charge transfer, a deeper understanding of the mechanisms governing interlayer coupling is still required. Therefore, we introduce a unified and physically

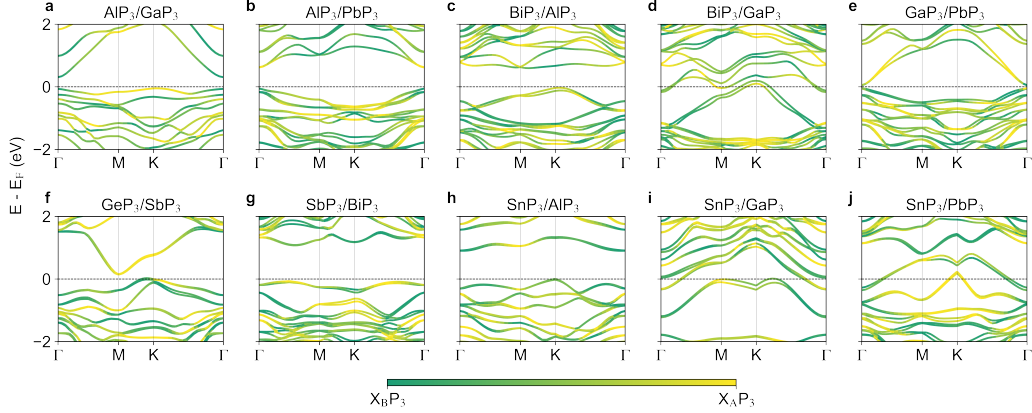


Figure 3: Layer-projected electronic band structures of representative XP_3 heterostructures: (a) AlP_3/GaP_3 , (b) AlP_3/PbP_3 , (c) BiP_3/AlP_3 , (d) BiP_3/GaP_3 , (e) GaP_3/PbP_3 , (f) GeP_3/SbP_3 , (g) SbP_3/BiP_3 , (h) SnP_3/AlP_3 , (i) SnP_3/GaP_3 , and (j) SnP_3/PbP_3 . The dashed horizontal line indicates the Fermi level set to zero energy. The color scale represents the relative contribution of each constituent monolayer to the electronic states, allowing identification of band localization and interlayer hybridization near the valence and conduction band edges.

grounded descriptor framework that distinguishes ionic, polar-covalent, and vdW-like interaction regimes and enables predictive screening of $X_A P_3/X_B P_3$ heterostructures based on their intrinsic atomic characteristics.

In this framework, the equilibrium metal-metal interlayer distance $d_{X_A X_B}$, the electron localization function (ELF) at the interface, and the Bader charge redistribution $\Delta\rho$ are employed as complementary descriptors of the interlayer interaction. Together, these quantities capture the geometric configuration of the interface, the degree of electronic localization, and the magnitude of interlayer charge transfer, providing a comprehensive description of the coupling mechanisms between stacked layers.

Within this framework, we analyze the interlayer interaction through the electron localization function evaluated at the midpoint of the interlayer metal-metal contact, denoted as ELF_{mid} . This quantity corresponds to the ELF value at the geometric midpoint of the equilibrium metal-metal interlayer distance $d_{X_A X_B}$, which defines the central region of the interface, as illustrated in Fig. 4(a). The use of ELF_{mid} is motivated by its direct sensitivity to electronic localization in the interfacial region where interlayer coupling is established. Unlike the Bader charge transfer $\Delta\rho$, which quantifies the net electron redistribution between layers, ELF_{mid} probes the degree of

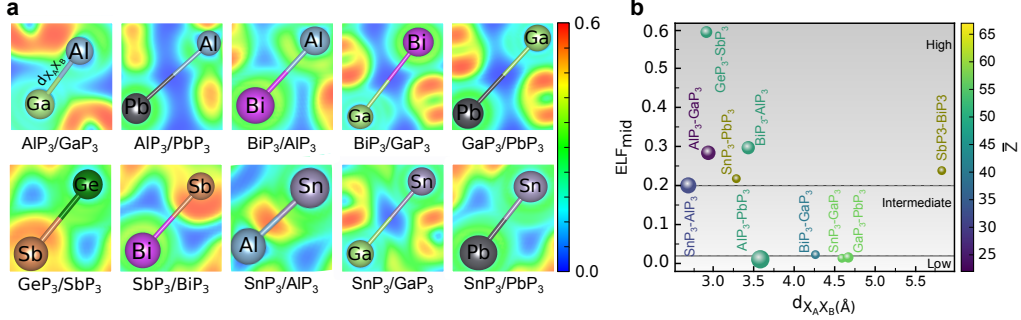


Figure 4: (a) Electron localization function (ELF) mapped along the interlayer direction across the interface, illustrating the spatial evolution of electronic localization between the stacked XP_3 monolayers. (b) Scatter plot of ELF_{mid} as a function of the equilibrium interlayer distance $d_{X_A X_B}$, where the marker size is proportional to the magnitude of the Bader charge transfer $|\Delta\rho|$, and the color scale represents the average atomic number \bar{Z} of the constituent metal atoms.

electronic sharing or depletion in real space, providing insight into whether the interaction is dominated by covalent overlap, ionic polarization, or weak dispersive forces.

By evaluating ELF specifically at the metal–metal midpoint, we focus on the region where orbital overlap and interfacial hybridization are maximized, making ELF_{mid} a direct indicator of the strength and character of interlayer electronic coupling. When combined with the Bader charge transfer $\Delta\rho$, which captures long-range electrostatic redistribution, this approach enables a unified and physically transparent classification of interaction regimes. In addition to these primary descriptors, the average atomic number \bar{Z} is considered as an auxiliary parameter to provide physical insight into deviations from the general $ELF_{\text{mid}} - \Delta\rho - d_{X_A X_B}$ trends. The obtained quantity values are summarized in Table 2.

To visualize the relationship between electronic localization and interlayer separation, Fig. 4(b) presents ELF_{mid} as a function of the equilibrium metal–metal interlayer distance $d_{X_A X_B}$. The size of the markers represents the magnitude of the Bader charge transfer $|\Delta\rho|$, while the color scale indicates the average atomic number \bar{Z} of the constituent elements.

Both ELF_{mid} and $\Delta\rho$ exhibit a clear inverse dependence on the equilibrium interlayer distance $d_{X_A X_B}$. High ELF_{mid} values (~ 0.20 – 0.60), together with substantial charge transfer, occur at short interlayer distances ($d_{X_A X_B} < 3.0$ Å), as observed for AlP₃/GaP₃ and SnP₃/AlP₃, characterizing ionic or polar–ionic

coupling. $\text{GeP}_3/\text{SbP}_3$ also lies in this short-distance regime but exhibits moderate charge redistribution combined with high ELF_{mid} , indicating a polar-covalent interaction dominated by electronic sharing. $\text{BiP}_3/\text{AlP}_3$, at an intermediate interlayer distance (3.42 Å), maintains a relatively high ELF_{mid} (0.31) together with moderate charge transfer, placing it in an intermediate polar-covalent regime. At larger separations ($d_{X_A X_B} > 3.5$ Å), most interfaces display both low ELF_{mid} (< 0.05) and small charge transfer, as in $\text{SnP}_3/\text{GaP}_3$, $\text{BiP}_3/\text{GaP}_3$, and $\text{GaP}_3/\text{PbP}_3$, consistent with vdW-like or weakly interacting interfaces. $\text{AlP}_3/\text{PbP}_3$ constitutes a clear exception, exhibiting very low ELF_{mid} despite a large charge transfer, which indicates a predominantly ionic interaction stabilized by long-range electrostatics rather than electronic overlap.

Notably, $\text{SnP}_3/\text{PbP}_3$ and $\text{SbP}_3/\text{BiP}_3$ stand out as distinctive cases in the high- \bar{Z} regime. Both interfaces are classified as vdW-like, albeit for different physical reasons: $\text{SnP}_3/\text{PbP}_3$ shows negligible charge transfer even at short distances, whereas $\text{SbP}_3/\text{BiP}_3$ retains a finite ELF_{mid} at large separations due to strong electronic polarization. The close agreement between the band structures calculated with and without SOC, as shown in Figs. S1 (g) and (j) of the Supplementary Material, indicates that these features arise primarily from orbital extension effects rather than from SOC.

Overall, the analysis demonstrates that both ELF_{mid} and $\Delta\rho$ are primarily governed by the equilibrium interlayer distance $d_{X_A X_B}$, although their dependence on this distance is not strictly monotonic. This establishes $d_{X_A X_B}$ as a natural first descriptor for initiating the search for interfaces with targeted interlayer coupling. Systematic deviations from the general $\text{ELF}_{\text{mid}}-\Delta\rho-d_{X_A X_B}$ trends are consistently explained by the average atomic number \bar{Z} , which captures electronic polarization and orbital extension effects beyond purely geometric considerations.

Taken together, these results define a simple and physically grounded screening framework for $X_A\text{P}_3/X_B\text{P}_3$ heterostructures. By selecting the constituent atoms X_A and X_B according to their atomic size and \bar{Z} , it is possible to preselect ionic, polar-covalent, or vdW-like coupling regimes at an early design stage. This provides a property-oriented basis for engineering interlayer interactions and guides the targeted design of XP_3 -based vertical heterostructures.

Heterobilayers	C_{11}	C_{12}	E	G	ν
AlP ₃ /GaP ₃	93.05	51.59	64.44	20.73	0.55
AlP ₃ /PbP ₃	55.53	49.11	12.09	3.21	0.88
BiP ₃ /AlP ₃	92.50	19.72	88.29	36.39	0.21
BiP ₃ /GaP ₃	90.27	26.58	82.44	31.84	0.29
GaP ₃ /PbP ₃	87.20	27.20	78.72	30.00	0.31
GeP ₃ /SbP ₃	127.24	17.45	124.85	54.90	0.14
SbP ₃ /BiP ₃	98.03	14.16	95.99	41.93	0.14
SnP ₃ /AlP ₃	89.50	31.02	78.75	29.24	0.35
SnP ₃ /GaP ₃	87.93	17.24	84.55	35.35	0.20
SnP ₃ /PbP ₃	74.80	16.49	71.16	29.15	0.22

Table 3: Calculated elastic constants (C_{11} and C_{12}) and derived mechanical properties, including Young’s modulus (E), shear modulus (G), and Poisson’s ratio (ν), for $X_A P_3/X_B P_3$ heterobilayers. Elastic constants and moduli are expressed in N/m, and Poisson’s ratio is dimensionless.

3.4. Elastic Properties

Having classified the XP_3 heterostructures according to their interfacial interaction regimes, we now examine how these regimes influence their elastic response. The calculated elastic constants and derived mechanical parameters are reported in Table 3. The mechanical behavior reflects the combined influence of interfacial bonding character and the equilibrium metal–metal separation. In all investigated systems, this separation varies from 2.69 to 5.82 Å, establishing a structural scale associated with the degree of interlayer coupling and its impact on in-plane stiffness.

Heterobilayers exhibiting ionic or polar–covalent interaction character, including SnP₃/AlP₃ (2.69 Å), GeP₃/SbP₃ (2.92 Å), AlP₃/GaP₃ (2.94 Å), BiP₃/AlP₃ (3.42 Å), and AlP₃/PbP₃ (3.55 Å), are characterized by comparatively shorter separations. Reduced distances favor enhanced orbital overlap and electrostatic interaction, which are generally associated with increased in-plane stiffness. Within this group, C_{11} ranges from 55.53 to 127.24 N/m, Young’s modulus from 12.09 to 124.85 N/m, and the shear modulus from 3.21 to 54.90 N/m. With the exception of AlP₃/PbP₃, which exhibits comparatively low rigidity, the remaining systems display higher elastic constants consistent with stronger interfacial coupling.

In contrast, heterobilayers classified as predominantly vdW-like, such as SnP₃/GaP₃ (4.24 Å), BiP₃/GaP₃ (4.59 Å), GaP₃/PbP₃ (4.64 Å), SnP₃/PbP₃

(3.28 Å), and SbP₃/BiP₃ (5.82 Å), generally exhibit larger separations and moderate elastic constants. In this regime, C_{11} varies between 74.79 and 98.03 N/m, Young’s modulus between 71.16 and 95.99 N/m, and the shear modulus between 29.15 and 41.93 N/m. The predominance of dispersive interactions in these systems is consistent with comparatively weaker interfacial mechanical coupling.

The partial overlap between the separation intervals (3.28–3.55 Å) indicates that metal–metal distance alone does not fully determine the elastic response. Within this intermediate range, electronic polarization, charge redistribution, and bonding directionality contribute to the observed variations in stiffness. For example, SnP₃/PbP₃ (3.28 Å) behaves as a vdW-like system despite its relatively short separation, whereas BiP₃/AlP₃ (3.42 Å) exhibits higher rigidity associated with stronger polar–covalent contributions. Similarly, AlP₃/PbP₃ (3.55 Å) deviates from a simple distance–stiffness correlation, presenting low Young’s modulus and high Poisson’s ratio, indicative of pronounced transverse strain coupling.

Overall, the equilibrium metal–metal separation serves as a primary structural descriptor correlated with interfacial stiffness, while the bonding regime and electronic structure effects modulate the mechanical response, particularly within the intermediate distance range. These results reinforce that geometric proximity and interfacial electronic character must be considered jointly when analyzing the elastic behavior of X_AP₃/X_BP₃ heterostructures.

3.5. Optical Properties

The optical response of XP₃ heterobilayers provides important insight into their potential for optoelectronic and photocatalytic applications. In 2D systems, reduced dielectric screening and interlayer electronic coupling can significantly modify light–matter interactions and enhance excitonic effects. To characterize the optical behavior of the XP₃ heterostructures under electromagnetic radiation, we analyze the absorption coefficient.

To illustrate the main optical trends, we focus on semiconducting heterobilayers with moderate band gaps, namely AlP₃/GaP₃ (0.35 eV), AlP₃/PbP₃ (0.67 eV), BiP₃/AlP₃ (0.61 eV), SbP₃/BiP₃ (1.11 eV), and SnP₃/AlP₃ (0.89 eV). Fig. 5 presents the absorption coefficient for the linear polarization directions xx and yy . The results reveal that these compounds are intrinsically anisotropic, exhibiting distinct optical responses depending on the polarization direction of the incident electric field. Furthermore, the XP₃ heterostructures begin to absorb in the infrared region and display pronounced peaks spanning

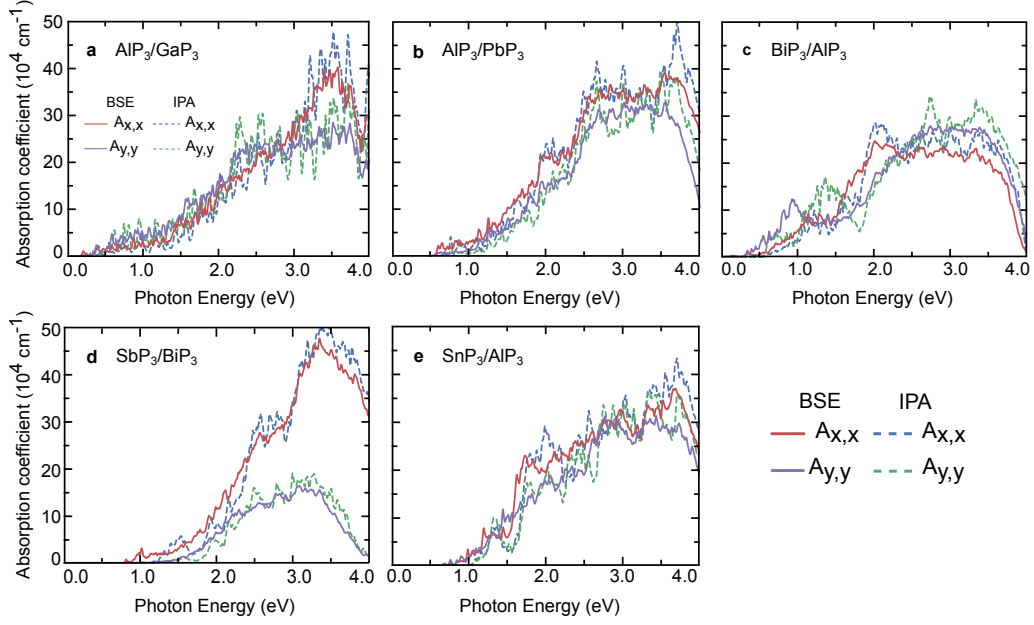


Figure 5: Absorption spectra of representative XP_3 heterostructures: (a) AIP_3/GaP_3 , (b) AIP_3/PbP_3 , (c) BiP_3/AIP_3 , (d) SbP_3/BiP_3 , and (e) SnP_3/AIP_3 . Solid curves correspond to spectra calculated within the Bethe–Salpeter Equation (BSE) formalism, while dashed curves represent the Independent Particle Approximation (IPA). Red and purple lines denote light polarized along the xx and yy directions.

the visible and ultraviolet energy ranges. Among the five heterobilayers studied, only the BiP_3/AIP_3 system exhibits a more pronounced absorption coefficient for light polarized along the yy direction. This behavior can be attributed to the orbital character of the states forming the valence and conduction band edges. When the contributing orbitals (s , p , and d) are preferentially oriented along a given crystallographic direction, the transition probability for photons polarized along that direction increases. In addition, structural anisotropy arising from lattice distortions or stacking configuration leads to an inequivalent electronic response along the x and y directions.[1]

Notably, AIP_3/GaP_3 , AIP_3/PbP_3 , BiP_3/AIP_3 , and SbP_3/BiP_3 are found to exhibit type-II band alignment (see Fig. 2). In these systems, the absorption spectra show relatively weak excitonic features near the band gap, characterized by discrete peaks and low absorption intensity. This behavior may be associated with the partial spatial separation of electrons and holes between adjacent layers. Similar effects have been reported in type-II heterostructures

such as MoSe₂-WSe₂. [28] Although a detailed analysis of the excitonic states is beyond the scope of the present work, this charge separation mechanism may be beneficial for photocatalytic applications.

3.6. Band-Edge Alignment for Photocatalysis

The photocatalytic performance of the Janus XP₃ heterostructures was evaluated through band edge alignment relative to the vacuum level, as shown in Fig. 2. The positions of the conduction band minimum (E_{CBM}) and valence band maximum (E_{VBM}) were compared with the pH-dependent redox potentials of water on the absolute energy scale. This approach allows assessment of the thermodynamic feasibility of the hydrogen evolution reaction (HER) and oxygen evolution reaction (OER).

The pH dependence of the redox potentials is described by the Nernst equations: [29]

$$E_{\text{HER}}(pH) = -4.44 + 0.059 pH \quad (\text{eV}), \quad (2)$$

$$E_{\text{OER}}(pH) = -5.67 + 0.059 pH \quad (\text{eV}). \quad (3)$$

For photocatalytic water splitting, the band edges of the semiconductor must straddle the redox potentials of water. The thermodynamic criteria for overall water splitting under single-photon excitation can be expressed as:

$$E_{\text{CBM}} > E_{\text{HER}}(pH), \quad (4)$$

$$E_{\text{VBM}} < E_{\text{OER}}(pH), \quad (5)$$

$$E_g \geq 1.23 \text{ eV}, \quad (6)$$

where 1.23 eV corresponds to the thermodynamic potential difference between HER and OER at standard conditions. At pH 0, 7, and 14, the redox levels shift according to the above relations, modifying the alignment conditions accordingly.

Fig. 2 indicates that seven heterobilayers exhibit semiconducting behavior, while three systems are metallic. Band alignment inferred from the isolated monolayers suggests two type-I systems, GeP₃/SbP₃ and SnP₃/AlP₃, and five type-II systems: AlP₃/GaP₃, AlP₃/PbP₃, BiP₃/AlP₃, GaP₃/PbP₃, and SbP₃/BiP₃. However, explicit calculations of the complete heterobilayers, as shown in Fig. 3, reveal band renormalization induced by interlayer interaction. In particular, GeP₃/SbP₃ transitions from a type-I alignment predicted for the

isolated monolayers to a type-II configuration in the fully relaxed heterobilayer, as shown in Fig. 3(f).

According to Eqs. 2 and 3, only SbP₃/BiP₃ exhibits a conduction band minimum (CBM) position compatible with the hydrogen evolution reaction (HER) within the investigated pH range, satisfying the HER criterion only under alkaline conditions. In contrast, all heterostructures meet the thermodynamic requirement for the oxygen evolution reaction (OER) throughout the considered pH window. Although some systems satisfy the band-edge alignment conditions for one or both half-reactions, their relatively small band gaps limit their suitability for spontaneous overall water splitting under single-photon excitation. [30, 31]

Within this context, among the studied XP₃ heterobilayers, AlP₃/PbP₃, BiP₃/AlP₃, and SbP₃/BiP₃ stand out as the most promising candidates for selective half-reactions, as their band alignment supports either hydrogen evolution or oxygen evolution depending on the pH conditions. These systems combine semiconducting character, moderate band gaps, and type-II band alignment, which facilitates spatial separation of photogenerated charge carriers and is advantageous for interfacial redox processes. [32, 33]

To further quantify the driving force behind this spatial separation, we evaluate the intrinsic internal field ($E_{\text{built-in}}$) within each junction using the electrostatic gradient formalism, $E_{\text{built-in}} = -\Delta V/H_{\text{total}}$. [34] Here, ΔV represents the potential drop between the topmost and bottommost vertical positions of the heterobilayer, and H_{total} denotes the total thickness, including the interlayer distance Δh . Notably, AlP₃/PbP₃ and BiP₃/AlP₃ exhibit the most robust internal fields in the series, reaching magnitudes of -4.09×10^7 V/m and 5.34×10^7 V/m, respectively. These values are of the same order of magnitude as those reported for high-performance 2D photocatalytic interfaces where strong internal fields are known to effectively suppress radiative recombination. [35, 36, 37] The calculated structural parameters, potential drops, and $E_{\text{built-in}}$ magnitudes for all investigated structures are compiled in the Table S1 of the Supplementary Material.

Materials that predominantly facilitate only one half-reaction may nevertheless remain relevant for practical implementations, for instance in the presence of sacrificial electron donors or within tandem and Z-scheme photocatalytic systems, where spatial separation of redox processes can improve the overall efficiency. [38, 39, 40, 41, 42] The present assessment focuses exclusively on thermodynamic band alignment, without considering kinetic limitations or reaction overpotentials.

4. Conclusion

In summary, we performed a first-principles investigation of vertical heterobilayers formed by XP_3 monolayers. The analyzed systems are energetically favorable and mechanically stable, confirming their viability as 2D heterostructures. The heterobilayers exhibit diverse electronic responses ranging from metallic and near-metallic to semiconducting regimes, with several systems displaying type-II band alignment that favors spatial separation of photo-generated carriers. Selected structures also present visible-to-near-infrared optical absorption and band-edge positions compatible with specific redox half-reactions, indicating potential for optoelectronic and photocatalytic applications.

To rationalize the interfacial interactions in these systems, we establish a physically grounded framework based on geometric and electronic descriptors that enables the classification and screening of coupling regimes as vdW-like, polar-covalent, or ionic in XP_3 heterostructures. Overall, this work establishes a physically grounded strategy for understanding and screening interfacial coupling regimes in XP_3 -based heterostructures. With appropriate adaptations, the descriptor-based approach introduced here can be extended to other classes of 2D interfaces, offering a general framework for the rational design and discovery of functional 2D heterostructures.

Acknowledgments

The authors acknowledge financial support from CNPq, FAPEMIG (including Rede-2D, grant RED-00079-23), FAPEMAT (PRO-2025/00376), INCT Materials Informatics, and INCT de Fotônica. T.A.S.P. and E.S.B. also acknowledge support from PDPG-FAPDF-CAPES Centro-Oeste (00193-00000867/2024-94). The authors further acknowledge the computational resources provided by LCC-UFLA, CENAPAD-SP, and LMCC-UFMT.

References

- [1] A. Castellanos-Gomez, X. Duan, Z. Fei, H. R. Gutierrez, Y. Huang, X. Huang, J. Querada, Q. Qian, E. Sutter, P. Sutter, Van der waals heterostructures, *Nature Reviews Methods Primers* 2 (1) (2022) 58.
- [2] Y. Jing, Y. Ma, Y. Li, T. Heine, [Gep3: A small indirect band gap 2d crystal with high carrier mobility and strong interlayer quantum](#)

- confinement, *Nano Letters* 17 (3) (2017) 1833–1838. doi:10.1021/acs.nanolett.6b05143.
URL <https://doi.org/10.1021/acs.nanolett.6b05143>
- [3] S. Yao, X. Zhang, Z. Zhang, A. Chen, Z. Zhou, 2d triphosphides: Sbp₃ and gap₃ monolayer as promising photocatalysts for water splitting, *International Journal of Hydrogen Energy* 44 (12) (2019) 5948–5954. doi:<https://doi.org/10.1016/j.ijhydene.2019.01.106>.
URL <https://www.sciencedirect.com/science/article/pii/S0360319919302381>
- [4] B. Ghosh, S. Puri, A. Agarwal, S. Bhowmick, Snp₃: A previously unexplored two-dimensional material, *The Journal of Physical Chemistry C* 122 (31) (2018) 18185–18191. doi:10.1021/acs.jpcc.8b06668.
URL <https://doi.org/10.1021/acs.jpcc.8b06668>
- [5] P. C. Donohue, H. S. Young, Synthesis, structure, and superconductivity of new high pressure phases in the systems gep and geas, *Journal of Solid State Chemistry* 1 (1970) 143–149. doi:10.1016/0022-4596(70)90005-8.
- [6] J. Gullman, O. Olofsson, The crystal structure of snp₃ and a note on the crystal structure of gep₃, *Journal of Solid State Chemistry* 5 (1972) 441–445. doi:10.1016/0022-4596(72)90091-6.
- [7] W. Qi, H. Zhao, Y. Wu, H. Zeng, T. Tao, C. Chen, C. Kuang, S. Zhou, Y. Huang, Facile synthesis of layer structured gep₃/c with stable chemical bonding for enhanced lithium-ion storage, *Scientific Reports* 7 (2017) 43582. doi:10.1038/srep43582.
- [8] M. Yan, B. Yang, X. Sun, Z. Wang, X. Jiang, W. Yi, H. Sun, R. Yang, H. Ding, D. Yue, K. Zhai, Y. Li, X. Chen, Y. Zhang, X. Liu, High quality 2d snp₃ nanosheets: Novel flexible electrode for energy storage device application with wide temperature adaptivity, *ACS Materials Letters* 6 (1) (2024) 194–202. doi:10.1021/acsmaterialslett.3c01438.
- [9] I. S. de Oliveira, E. N. Lima, R. H. Miwa, D. Pacine, Unveiling the electronic properties of bip₃ triphosphide from bulk to graphene-based heterostructures by first-principles calculations, *Applied Surface Science* 662 (2024) 160041.

doi:<https://doi.org/10.1016/j.apsusc.2024.160041>.

URL <https://www.sciencedirect.com/science/article/pii/S0169433224007542>

- [10] B. Lu, X. Zheng, Z. Li, [Two-dimensional lateral heterostructures of triphosphides: Alp₃-gap₃ as a promising photocatalyst for water splitting](#), ACS Applied Materials & Interfaces 12 (48) (2020) 53731–53738, pMID: 33205943. [arXiv:https://doi.org/10.1021/acsami.0c13700](https://doi.org/10.1021/acsami.0c13700), doi:10.1021/acsami.0c13700.
URL <https://doi.org/10.1021/acsami.0c13700>
- [11] P. Hohenberg, W. Kohn, [Inhomogeneous electron gas](#), Phys. Rev. 136 (1964) B864–B871. doi:10.1103/PhysRev.136.B864.
URL <https://link.aps.org/doi/10.1103/PhysRev.136.B864>
- [12] W. Kohn, L. J. Sham, [Self-consistent equations including exchange and correlation effects](#), Phys. Rev. 140 (1965) A1133–A1138. doi:10.1103/PhysRev.140.A1133.
URL <https://link.aps.org/doi/10.1103/PhysRev.140.A1133>
- [13] G. Kresse, J. Furthmüller, [Efficient iterative schemes for ab initio total-energy calculations using a plane-wave basis set](#), Phys. Rev. B 54 (1996) 11169–11186. doi:10.1103/PhysRevB.54.11169.
URL <https://link.aps.org/doi/10.1103/PhysRevB.54.11169>
- [14] J. P. Perdew, K. Burke, M. Ernzerhof, [Generalized gradient approximation made simple](#), Phys. Rev. Lett. 77 (1996) 3865–3868. doi:10.1103/PhysRevLett.77.3865.
URL <https://link.aps.org/doi/10.1103/PhysRevLett.77.3865>
- [15] G. Kresse, D. Joubert, [From ultrasoft pseudopotentials to the projector augmented-wave method](#), Phys. Rev. B 59 (1999) 1758–1775. doi:10.1103/PhysRevB.59.1758.
URL <https://link.aps.org/doi/10.1103/PhysRevB.59.1758>
- [16] S. Grimme, J. Antony, S. Ehrlich, H. Krieg, [A consistent and accurate ab initio parametrization of density functional dispersion correction \(dft-d\) for the 94 elements h-pu](#), The Journal of chemical physics 132 (15) (2010).

- [17] H. J. Monkhorst, J. D. Pack, [Special points for brillouin-zone integrations](#), Phys. Rev. B 13 (1976) 5188–5192. doi:10.1103/PhysRevB.13.5188. URL <https://link.aps.org/doi/10.1103/PhysRevB.13.5188>
- [18] J. Heyd, G. E. Scuseria, M. Ernzerhof, Hybrid functionals based on a screened coulomb potential, Journal of Chemical Physics 118 (2003) 8207–8215. doi:10.1063/1.1564060.
- [19] J. Heyd, G. E. Scuseria, M. Ernzerhof, Erratum: Hybrid functionals based on a screened coulomb potential, Journal of Chemical Physics 124 (2006) 219906. doi:10.1063/1.2204597.
- [20] A. C. Dias, J. F. Silveira, F. Qu, [Wantibexos: A wannier based tight binding code for electronic band structure, excitonic and optoelectronic properties of solids](#), Computer Physics Communications 285 (2023) 108636. URL <http://dx.doi.org/10.1016/j.cpc.2022.108636>
- [21] A. C. Dias, J. F. Silveira, F. Qu, [An updated version of wannier90: A tool for obtaining maximally-localised wannier functions](#), Computer Physics Communications 185 (2014) 2309. URL <http://dx.doi.org/10.1016/j.cpc.2014.05.003>
- [22] C. A. Rozzi, D. Varsano, A. Marini, E. K. U. Gross, A. Rubio, [Exact coulomb cutoff technique for supercell calculations](#), Physical Review B 73 (2006) 1550–235X. URL <http://dx.doi.org/10.1103/PhysRevB.73.205119>
- [23] E. E. Salpeter, H. A. Bethe, [A relativistic equation for bound-state problems](#), Physical Review 84 (1951) 1232. URL <http://dx.doi.org/10.1103/PhysRev.84.1232>
- [24] M. S. Ramzan, V. Bacic, Y. Jing, A. Kuc, Electronic properties of a new family of layered materials from groups 14 and 15: first-principles simulations, The Journal of Physical Chemistry C 123 (41) (2019) 25470–25476.
- [25] G. E. Gama Araujo, L. Moraes Gomes, D. Pacine de Andrade Deus, A. C. Dias, A. L. da Rosa, Dispersive and flat electronic bands in two-dimensional triphosphides, ACS Applied Energy Materials 8 (15) (2025) 11548–11560.

- [26] R. F. W. Bader, *Atoms in Molecules - A Quantum Theory*, Oxford University Press, Oxford, 1990.
- [27] G. Henkelman, A. Arnaldsson, H. Jónsson, A fast and robust algorithm for bader decomposition of charge density, *Comput. Mater. Sci.* 36 (3) (2006) 354–360.
- [28] P. Rivera, J. R. Schaibley, A. M. Jones, J. S. Ross, S. Wu, G. Aivazian, P. Klement, K. Seyler, G. Clark, N. J. Ghimire, J. Yan, D. G. Mandrus, W. Yao, X. Xu, [Observation of long-lived interlayer excitons in monolayer mose2–wse2 heterostructures](https://doi.org/10.1038/ncomms7242), *Nature Communications* 6 (1) (Feb. 2015). doi:10.1038/ncomms7242.
URL <http://dx.doi.org/10.1038/ncomms7242>
- [29] A.-S. Feiner, A. McEvoy, The nernst equation, *Journal of chemical education* 71 (6) (1994) 493.
- [30] L. Quan, H. Jiang, G. Mei, Y. Sun, B. You, Bifunctional electrocatalysts for overall and hybrid water splitting, *Chemical Reviews* 124 (7) (2024) 3694–3812.
- [31] A. Raveendran, M. Chandran, R. Dhanusuraman, A comprehensive review on the electrochemical parameters and recent material development of electrochemical water splitting electrocatalysts, *RSC advances* 13 (6) (2023) 3843–3876.
- [32] Z. Xi, M. Liu, Advancing photoelectrochemical systems for sustainable energy and chemical production: challenges and opportunities, *npj Materials Sustainability* 3 (1) (2025) 18.
- [33] Y.-C. Lin, P. Wyzga, J. Macyk, W. Macyk, M. N. Guzik, Solar-driven (photo) electrochemical devices for green hydrogen production and storage: Working principles and design, *Journal of Energy Storage* 82 (2024) 110484.
- [34] D. A. Neamen, *Semiconductor Physics and Devices: Basic Principles*, 5th Edition, McGraw-Hill Education, New York, NY, 2021, see Chapter 7: The pn Junction for the theoretical derivation of built-in electric fields and potential barriers.

- [35] L. Li, J. Ling, D. Zhang, N. Wang, J. Lin, Z. Xi, W. Xu, [Direct measurement of built-in electric field inside a 2d cavity](#), The Journal of Chemical Physics 160 (1) (2024) 011102. [arXiv:https://pubs.aip.org/aip/jcp/article-pdf/doi/10.1063/5.0180444/19664613/011102_1_5.0180444.pdf](#), doi:10.1063/5.0180444. URL <https://doi.org/10.1063/5.0180444>
- [36] H. Wang, D.-R. Chen, Y.-C. Lin, P.-H. Lin, J.-T. Chang, J. Muthu, M. Hofmann, Y.-P. Hsieh, [Enhancing the electrochemical activity of 2d materials edges through oriented electric fields](#), ACS Nano 18 (30) (2024) 19828–19835. doi:10.1021/acsnano.4c06341. URL <https://doi.org/10.1021/acsnano.4c06341>
- [37] J. Zhou, M. Zhang, B. Ren, Q. Yi, H. Yu, B. Zhang, A. Li, X. Hu, Z. Li, G. Chen, Y. Cheng, R. Gao, Y. Luan, J. Zhang, Y. Wang, Y. Hu, Z. Yang, B. Liang, H. Hao, J. Z. Ou, [Interfacial built-in electric field in 2d ni\(oh\)₂ heterojunction with the sodium organic compound for enhanced oxygen evolution catalysis](#), Chemical Engineering Journal 503 (2025) 158565. doi:<https://doi.org/10.1016/j.cej.2024.158565>. URL <https://www.sciencedirect.com/science/article/pii/S1385894724100563>
- [38] F. Costantino, P. V. Kamat, [Do sacrificial donors donate h₂ in photocatalysis?](#), ACS Energy Letters 7 (1) (2021) 242–246.
- [39] J. Schneider, D. W. Bahnemann, [Undesired role of sacrificial reagents in photocatalysis](#) (2013).
- [40] Y. Pellegrin, F. Odobel, [Sacrificial electron donor reagents for solar fuel production](#), Comptes Rendus Chimie 20 (3) (2017) 283–295.
- [41] S. Ghasemi, A. Parastesh, M. Padervand, H. Ren, X. Li, A. Labidi, M. Signoretto, E. A. Dawi, T. Hamzehlouyan, E. Lichtfouse, et al., [Recent progress on z-and s-scheme photocatalysis: mechanistic understanding toward green applications](#), Current Opinion in Chemical Engineering 47 (2025) 101059.
- [42] H. Fu, Y. Wu, Y. Guo, T. Sakurai, Q. Zhang, Y. Liu, Z. Zheng, H. Cheng, Z. Wang, B. Huang, et al., [A scalable solar-driven photocatalytic system](#)

for separated h₂ and o₂ production from water, Nature Communications
16 (1) (2025) 990.